FINAL PROGRESS REPORT

SPECT ASSAY OF RADIOLABELED MONOCLONAL ANTIBODIES

MAY 2001 - AUGUST 2004

Ronald J. Jaszczak, Ph.D.

Department of Radiology
Duke University Medical Center

and

Department of Biomedical Engineering
Duke University

Durham, North Carolina 27710

August 30, 2004

PREPARED FOR THE U.S. DEPARTMENT OF ENERGY
UNDER GRANT NUMBER DE-FG02-96ER62150

Report Number: DOE/ER/62150-5

I. INTRODUCTION

The therapeutic potential of radiolabeled monoclonal antibodies (MAbs) administered by compartmental routes is being investigated by several groups, and the initial results are quite encouraging. During the final project period, significant progress has been achieved in imaging high-energy localized activity distributions, such as those found in brain tumors. The goal of this project is to improve the capability of single photon emission computed tomography (SPECT) to accurately quantify the biodistribution of radiolabeled MAbs.

At the time of the last Renewal cycle, three years of support were requested, but two years of support were awarded by the DOE. This project period commenced 1 December 2001. As a result of the elimination of available funding for Year 3 and the reduction in the level of funding for Years 1 and 2, it was necessary to reduce the scope of the proposed research as follows:

We proposed to markedly reduce the research aimed at extending the capabilities of parallel-beam collimation for quantitative high-resolution imaging of whole body distributions of therapeutic doses of I-131-labeled MAbs. Specifically, we proposed to defer the design and construction of the proposed application-specific parallel hole collimator.

We proposed to focus our research efforts on collaborating closely with Jefferson National Accelerator Facility (JLab) to design, build and evaluate a compact, ultra-high-resolution, high-sensitivity gamma camera for quantifying brain-tumor distributions of I-131.

We also proposed to continue our on-going research in developing and evaluating pinhole collimation for quantitative ultra-high-resolution imaging of I-131-labeled MAbs.

We have made excellent progress in accomplishing much of the research related to pinhole collimation. Many of the most significant results have been presented in peer-reviewed journal articles and conference proceeding *[1-6]* (also see Section II.A).

We have also made good progress in collaborating with JLab's Detector Group in developing a compact, ultra-high-resolution, gamma camera. The prototype I-131 imager was delivered to Duke on May 28, 2003. An initial evaluation of this system has been performed during this project period.

II. PROGRESS REPORT

A.1. PUBLICATIONS SUPPORTED FULLY OR MAINLY BY THIS GRANT SINCE THE APPLICATION WAS LAST SUBMITTED FOR COMPETITIVE RENEWAL (MAY 2001 – MAY 2003)

1. Gonzàlez Trotter DE, Jaszczak RJ, Bowsher JE, Akabani G, Greer KL. High-resolution absolute SPECT quantitation for I-131 distributions used in the treatment of lymphoma: a phantom study. *2000 IEEE Nuclear Science Symposium Conference Record*, (October 15-20, 2000, Lyon, France), ISBN 0-7803-6506-2, pp. 18_2 – 18_6, 2001.
2. Gonzàlez Trotter DE, Bowsher JE, Jaszczak RJ. Improved I-131 SPECT resolution through modeling individual medium-energy collimator holes. *2000 IEEE Nuclear Science Symposium Conference Record*, (October 15-20, 2000, Lyon, France), ISBN 0-7803-6506-2, pp. 22-12-22-15, 2001.
3. Gonzàlez Trotter DE, Jaszczak RJ, Bowsher JE, Akabani G, Greer KL. High-resolution absolute SPECT quantitation for I-131 distributions used in the treatment of lymphoma: a phantom study. *IEEE Trans Nucl Sci*. 2001 ;48(3):707-14.
4. Tenney CR, Tornai MP, Smith MF, Turkington TG, Jaszczak RJ. Uranium pinhole collimators for 511-keV photon SPECT imaging of small volumes. *IEEE Trans Nucl Sci.* 2001 Apr;48(4):1483-9.
5. Metzler SD, Bowsher JE, Smith MF, Jaszczak RJ. Analytic determination of pinhole collimator sensitivity with penetration. *IEEE Trans Med Imag.* 2001 ;20(8):730-41.
6. Metzler SD, Bowsher JE, Greer KL, Jaszczak RJ. Analytic determination of the pinhole collimator's point-spread function and RMS resolution with penetration. *2001 IEEE Nuclear Science Symposium Conference Record*, (November 4-10, 2001, San Diego, CA), ISBN 0-7803-7326-X (CD-ROM), 2002.
7. Metzler SD, Bowsher JE, Greer KL, Jaszczak RJ. Analytic determination of the pinhole collimator's point-spread function and RMS resolution with penetration. *IEEE Trans Med Imag*. 2002 ;21(8):878-887.
8. Metzler SD, Bowsher JE, Jaszczak RJ. Geometrical similarities of the Orlov and Tuy sampling criteria and a numerical algorithm for assessing sampling completeness. *2002 IEEE Nuclear Science Symposium Conference Record*, (November 10-16, 2002, Norfolk, VA), ISBN 0-7803-7637-4 (CD-ROM), 2003.
9. Bowsher JE, Gonzalez Trotter DE, Jaszczak RJ. Modeling thick septa and utilizing unsummed rotating-collimator projections in iterative reconstruction for SPECT. *IEEE Trans Nucl Sci*, submitted, 2004.

B. JLAB-DUKE DEDICATED BRAIN-TUMOR IMAGING SYSTEM

B.1. Determination of Optimal Collimator Design

During the final project period a prototype I-131 dedicated brain imager has been designed and built. Several potential parallel hole collimator designs were considered. Computer simulations and analysis of alternate designs were performed at Duke to determine an optimal collimator design. Collimator response was characterized by spatial resolution and sensitivity. Both geometric (non-penetrative) and penetrative sensitivities were considered in selecting an optimal collimator design. For this simulation, a planar sheet source 1.65cm x 1.65cm was placed 10.0cm above the front collimator surface. The collimator was simulated to be made of lead ($\mu = 0.316mm^{-1}$). Collimator designs using different hole lengths were simulated. The values for the hole diameter presented in the column entitled "Constant-Resolution Hole Diameter" correspond to the hole diameters that would produce a constant-resolution value of 4.14mm for the different hole lengths. In practice, it is not possible to manufacture a real collimator with all such hole diameters; therefore, collimators with actual hole diameters that can be manufactured were used for the simulations. These hole diameters were equal to 1.46mm and 1.00mm. The center-to-center spacing of the holes was 3.3mm. The results of this simulation are shown in Table B1. Based on these results, two collimator designs were selected and built by external sources. One collimator has 1.5mm hexagonally shaped holes and a hole length of 40mm. This collimator was made by Nuclear Fields, Inc. (Des Plaines, IL) using their proprietary micro-casting methodology. The second collimator has 1mm round holes with the same hole pitch of 3.3mm. This is a machined collimator built by Vulcan Lead (Milwaukee, WI) and is comprised of a stack of up to five layers; each layer is 12.7mm thick. The initial results shown in this progress report were all obtained using the Nuclear Fields collimator, since the Vulcan collimator has not yet been delivered.

Table B1. Resolutions and Sensitivities of Potential I-131 Collimator Designs.

Actual Hole Length (mm)	Effective Hole Length (mm)	Constant-Resolution Hole Diameter (mm)	Calculated Constant-Resolution (mm)	Actual Hole Diameter (mm)	Actual Spatial Resolution (mm)	Total Sensitivity S(total)	Geometric Sensitivity S(Geometric)	Penetrative Sensitivity S(Penetrative)
64.00	57.67	1.46	4.14	1.46	4.14	7.64E-006	4.97E-006	2.68E-006
50.00	43.67	1.21	4.14	1.46	5.00	1.20E-005	7.63E-006	4.32E-006
50.00	43.67	1.21	4.14	1.00	3.43	5.50E-006	2.08E-006	3.42E-006
40.00	33.67	1.00	4.14	1.00	4.15	7.47E-006	3.04E-006	4.43E-006
37.50	31.17	.94	4.14	1.00	4.40	8.32E-006	3.41E-006	4.92E-006
30.00	23.67	.76	4.14	1.00	5.48	1.47E-005	4.72E-006	9.98E-006
25.00	18.67	.62	4.14	1.00	6.68	3.50E-005	6.38E-006	2.86E-005
20.00	13.67	.47	4.14	1.00	8.75	1.31E-004	9.20E-006	1.22E-004
15.00	8.67	.31	4.14	1.00	13.22	6.60E-004	1.57E-005	6.44E-004
12.50	6.17	.23	4.14	1.00	18.18	1.57E-003	2.20E-005	1.55E-003

B.2. Development Status of the Dedicated Brain Imager System

The prototype I-131 imaging system is composed of the following main components:

- detector head
- dedicated I-131 collimator
- x-y detector head scanner
- heavy mobile table to carry the detector, collimator and screening lead bricks wall
- cabinet for computer, DAQ VME crate, and UPS/isolation transformer unit
- rotating stage for initial phantom evaluations

B.3. Examples of the initial detector characterization

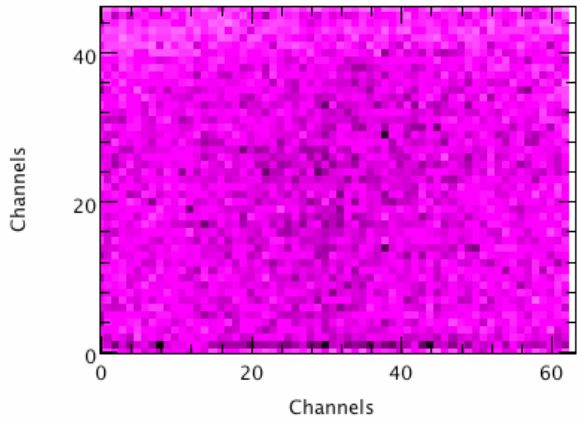

Figure B1. Example of a flood image obtained with a ^{57}Co source, after crystal pixel map linearization.

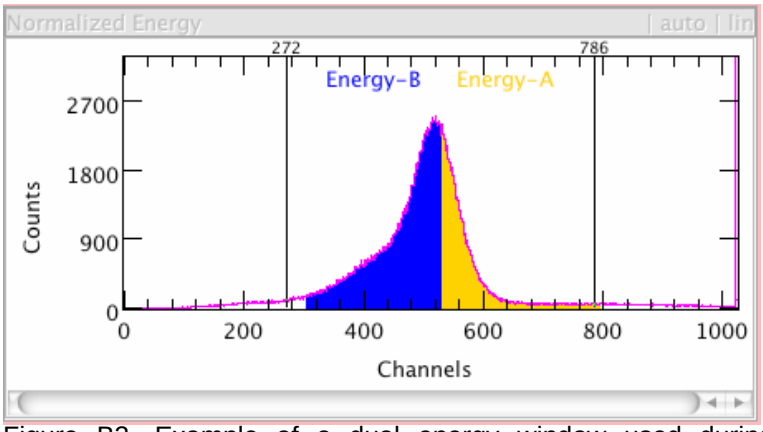

Figure B2. Example of a dual energy window used during ~uniform (flood) detector surface illumination with a ^{57}Co source, after amplitude normalization of all 2961 scintillation pixels.

An example of a raw image obtained on this detector equipped with a 6"x8" NaI(Tl) pixellated scintillator array with 47x63 3x3x19mm pixels with a 3.2mm pitch is shown in Figure B8. A non-collimated Na-22 point source was used to flood the scintillator array. All 2961 3mm pixels are seen well separated, including the ones from the gap regions between the individual PSPMTs.

Figure B1 shows a flood source image after linearity correction. A Co-57 (122 keV) source was used. The image demonstrates reasonably good uniformity of response. Figure B2 shows a sample energy spectrum acquired using a Co-57 flood source. The pulse heights from all 2961 scintillation crystals have been normalized. The potential use of two energy windows is also illustrated in this figure. Figure B3 shows a planar image of two Co-57 point sources. The point sources were placed 10cm in from the front surface of the I-131 collimator. Figure B4 shows an example of a reconstructed SPECT image of the two Co-57 point sources.

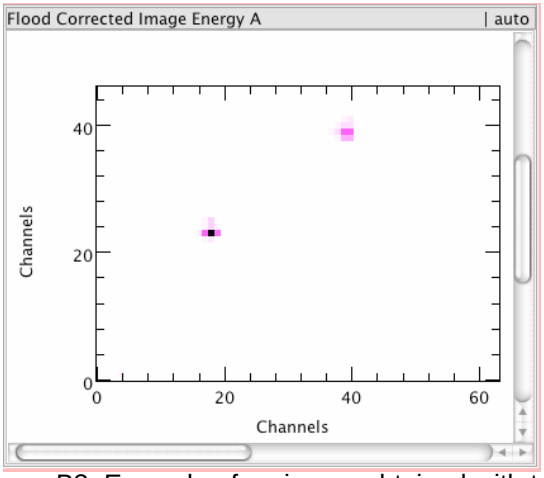

Figure B3. Example of an image obtained with two point 57Co sources placed 10cm in front of the I-131 collimator.

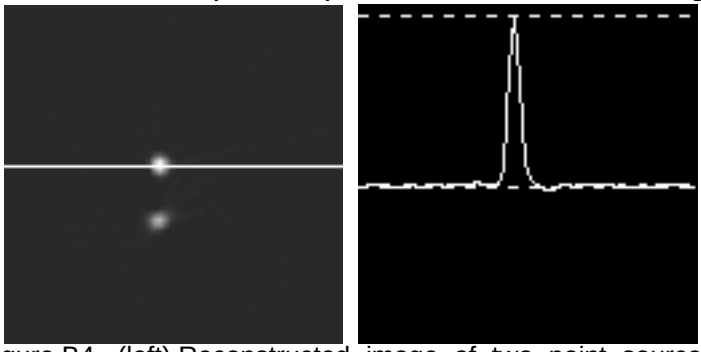

Figure B4. (left) Reconstructed image of two point sources. (right) Profile through image of upper point source.

C. Initial Development of SPECT Reconstruction Software for JLab-Duke Camera

C.1. Modeling Thick Septa and Collimator Holes: Geometrical-Phantom Study

A geometrical phantom designed to illuminate spatial resolution effects is shown in Figure C1. The phantom includes a uniformly attenuating medium that consists of all voxels within an elliptical cylinder that is centered on the axis of rotation, infinitely long, and with minor and major diameters of 15.0 and 22.0cm. The voxels are cubic and 0.100cm wide. The activity distribution is specified on a grid of 0.025-cm-wide voxels, and 4x4x4 sets of 0.025-cm-wide voxels are then summed to generate the activity distribution shown in Figure C1 on 0.100-cm-wide voxels. The activity distribution is contained within a smaller circular cylinder that is 2.0cm long and 3.7cm in diameter. The smaller cylinder is shifted 2.6cm from the center of rotation (1.8385cm in the horizontal and vertical directions). Within the cylinder, there are tubes of zero activity. The tubes are positioned on a hexagonal lattice and are separated center-to-center by 0.8cm. Each tube is 0.4cm in diameter.

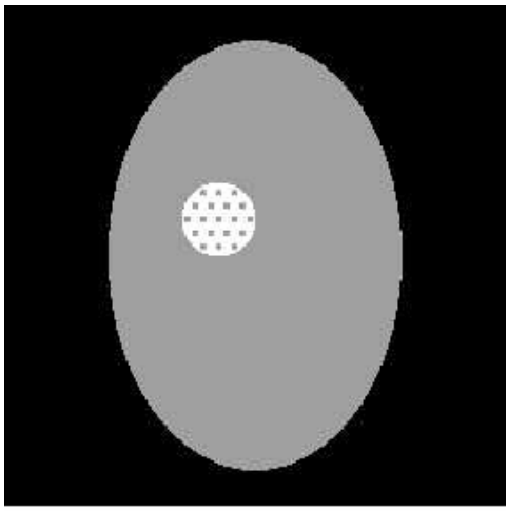

Figure C1. An overlay of the activity and attenuation distributions for the geometrical phantom. The larger 15.0x22.0-cm-diameter ellipse indicates the attenuating medium. Activity is contained within the 3.7-cm-diameter circle shown. The inactive, small, circular tubes are 0.4cm in diameter and are separated center-to-center by 0.8cm.

Figure C2 shows a zoom in on computer-simulated projections of the phantom in Figure C1. These computer simulations model a 6.4-cm-thick collimator with hexagonal holes that are 0.145cm wide, flat-to-flat. The holes are separated center-to-center by 0.345cm. The simulations model the spatially-varying spatial resolution corresponding to these holes, and they model a 2D-Gaussian shaped detector spatial resolution with a 0.30cm full-width-at-half-maximum (FWHM). The gamma camera orbit is circular, with a 12cm radius of rotation for the patient-side surface of the collimator. Figure C2(a) corresponds to the projections for one of the three angle settings of the rotating parallel hole collimator developed in *[7]*. The thick septa create a periodic and strong variation in sensitivity across the surface of the gamma camera, as is evident in these projections. Figure C2(b) shows the sum of the projections in (a) with two additional projections (not shown) in which the collimator has been rotated by 120 and 240 degrees about the collimator center. This summation greatly reduces the variation in sensitivity. Figure C2(c) shows "ideal" projections that would result from averaging over all displacements of the collimator within the plane of the collimator surface. (This is simulated by averaging over a hexagonal lattice of 0.04cm displacements across the 2D plane of the detector surface.) These projections are ideal in the sense that the high spatial resolution resulting from the thick septa is maintained, while uniform gamma camera sensitivity is also achieved. Hence, Figure C2(c) represents the intended ideal outcome of the rotation-and-sum procedure underlying Figure C2(b).

Image reconstructions from these noise-free projections are shown in Figures C3 and C4. The reconstructions are compared for equal computation times. These figures show that when the thick septa

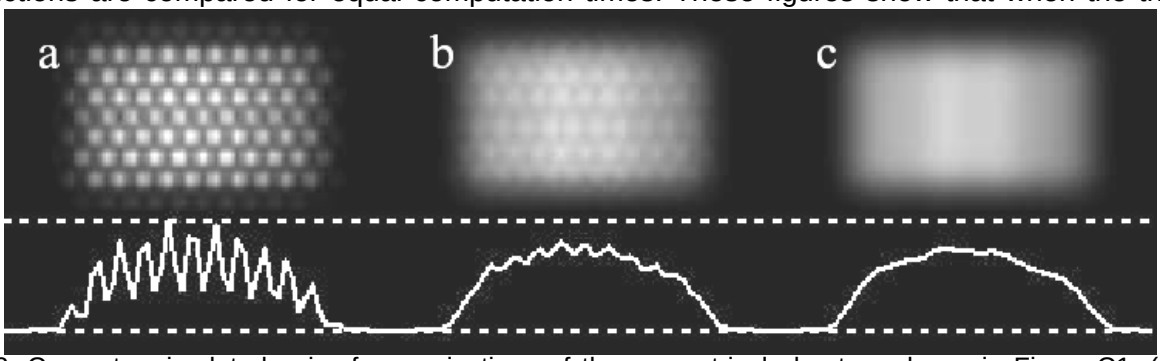

Figure C2. Computer-simulated noise-free projections of the geometrical phantom shown in Figure C1. (a) Noise-free projections obtained at one of the three rotation stops of the rotating parallel-hole collimator. (b) Sum of the projection shown in (a) with two additional projections (not shown) in which the collimator has been rotated by 120 and 240 degrees about the collimator center. (c) Projection that would be obtained by averaging over all possible displacements of the collimator within the plane of the collimator surface.

are not modeled within image reconstruction, approximately the same results are obtained using the summed data of Figure C2(b) as using the ideally spatially invariant projections of Figure C2(c). Hence these results are consistent with those in *[7-9]*, where good image quality was obtained using summed rotating collimator projections together with standard filtered back-projection (FBP) and iterative reconstruction methods that do not model the thick septa. Figures C3 and C4 show superior spatial resolution recovery when the projections of Figure C2(a) and the projections for the corresponding 120- and 240-degree rotations are left unsummed and the thick septa are modeled within image reconstruction.

C.2. Modeling Thick Septa and Collimator Holes: Hoffman Brain Phantom Study

Figure C5 shows computer-simulated projections of the 3D Hoffman brain phantom, and Figure C6 shows reconstructed images. The layouts of projections and images are similar to those for the geometrical phantom of the previous section and are described in the figure captions.

The phantom was implemented on 0.1-cm-wide cubical voxels. The orbit of the gamma camera was circular with a 14cm radius of rotation for the patient-side surface of the collimator. Attenuation effects were not modeled. Other projection simulation parameters were the same as those described above for the geometrical phantom.

Figure C6 shows reconstructed images for a high number of iterations with OSEM. At these high iteration numbers, and with the extended Hoffman brain phantom radiopharmaceutical distribution, artifacts

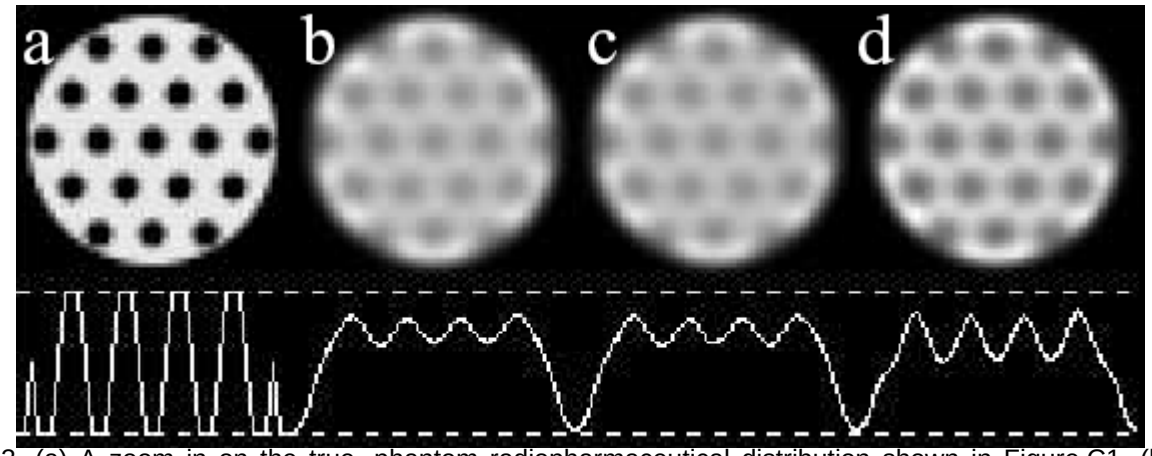

Figure C3. (a) A zoom in on the true, phantom radiopharmaceutical distribution shown in Figure C1. (b) OSEM reconstruction (6 iterations, 8 subsets) applied to the noise-free summed projection data shown in Figure C2(b). (c) OSEM reconstruction (6 iterations, 8 subsets) applied to the noise-free translationally averaged projection data shown in Figure C2(c). (d) OSEM reconstruction (2 iterations, 8 subsets) applied to the three noise-free unsummed projections acquired by the three rotation stops of the rotating parallel hole collimator. Figure C2(a) shows one of these three projections. The computation times for (b) and (c) are comparable to that for (d), since (d) involves one third the number of iterations but three times more projection data. As shown, method (d) provides better spatial resolution recovery in the same computation time. The profile is through the center of the images.

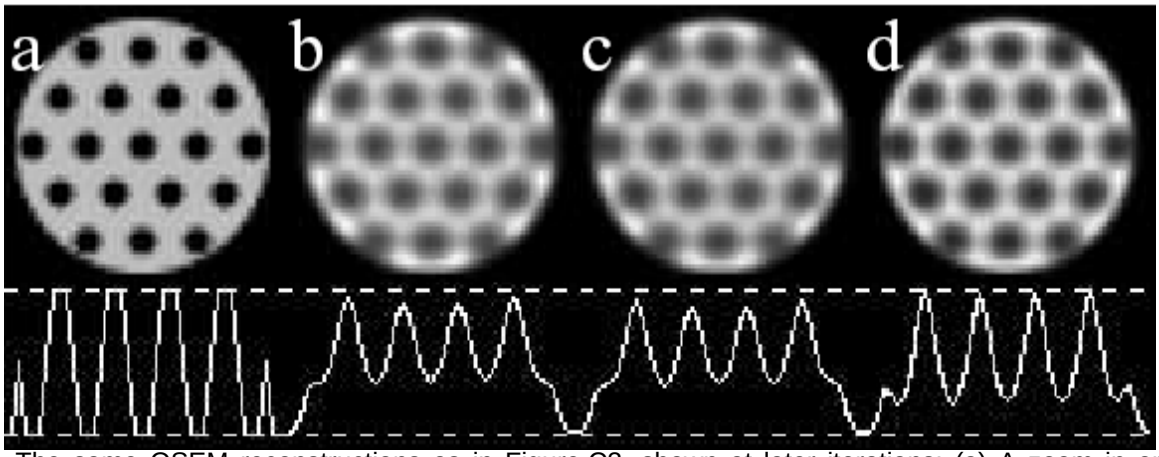

Figure C4. The same OSEM reconstructions as in Figure C3, shown at later iterations: (a) A zoom in on the true, phantom radiopharmaceutical distribution shown in Figure 1. (b-c) 30 iterations, 8 subsets (d) 10 iterations, 8 subsets.

are apparent in the reconstruction of summed data using standard OSEM without any modeling of thick septa. Presumably the artifacts arise because the reconstruction algorithm does not model the spatial variations in gamma camera response that are apparent in the projections of Figure C5(b). Notably, there are no such artifacts in the reconstruction shown in Figure C6(d), since this reconstruction *does* model the spatial variations seen in Figure C5(a). Similar to the results for the geometrical phantom, Figure C6 shows superior spatial resolution recovery from using unsummed projections and modeling the thick septa within image reconstruction.

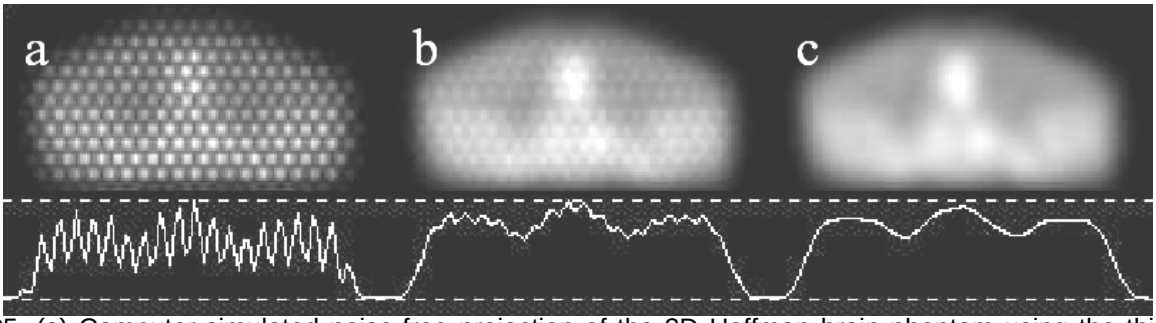

Figure C5. (a) Computer-simulated noise-free projection of the 3D Hoffman brain phantom using the thick-septa rotating collimator. (b) Sum of the projection shown in (a) with two additional projections (not shown) in which the collimator has been rotated by 120 and 240 degrees about the collimator center. (c) Computer-simulated noise-free projection of the 3D Hoffman brain phantom obtained by averaging over all possible displacements of the collimator within the plane of the collimator surface.

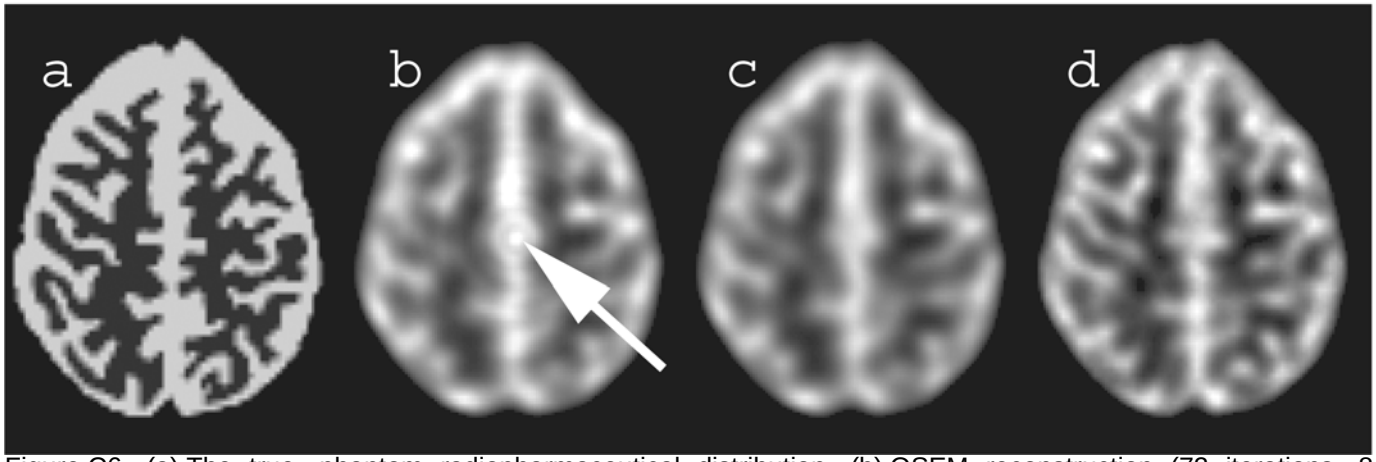

Figure C6. (a) The true, phantom radiopharmaceutical distribution. (b) OSEM reconstruction (72 iterations, 8 subsets) applied to the noise-free summed projection data shown in Figure C5(b). At this high number of iterations and with an extended radiopharmaceutical distribution, artifacts are apparent (for example, near arrow). The artifacts presumably arise because the spatial variation in gamma camera sensitivity is not modeled in the image reconstruction. (c) OSEM reconstruction (72 iterations, 8 subsets) applied to the noise-free translationally averaged projection data shown in Figure C5(c). (d) OSEM reconstruction (24 iterations, 8 subsets) applied to the three noise-free unsummed projections acquired by the three rotation stops of the rotating parallel hole collimator. Figure C5(a) shows one of these three projections. This image (d) has superior spatial resolution recovery compared to (b) and (c). Furthermore, image (d) does not show the artifacts present in (b) near arrow, since the spatial variation in gamma camera sensitivity is modeled in the reconstruction of (d).

D. PINHOLE POINT-RESPONSE FUNCTION (PRF) AND ROOT-MEAN-SQUARE (RMS) NOISE

During the previous project period, we developed an accurate analytic expression to determine the sensitivity of pinhole collimation that included the effects of penetration *[1]*. During the final project period, we have developed an accurate model of the point-response function of pinhole collimators *[5]*. That model is described below.

A knife-edge pinhole collimator can be modeled as two infinite back-to-back cones intersecting at the aperture. This model is fully characterized by the diameter d of the aperture and the acceptance angle α (Figure D1) of the cones. The plane of the aperture is the $z=0$ plane. The imaging plane is a distance b below the aperture. The circular aperture of diameter d is centered at $(x,y)=(0,0)$. The location of a photon point source at spherical coordinates (θ,ϕ) can be represented in rectangular coordinates as $(h\cot\theta\cos\phi, h\cot\theta\sin\phi, h)$. [The angle θ is the angle between the line segment from the center of the aperture to the photon source and its projection onto the plane of the aperture. The angle ϕ (not shown in Figure D1) is the azimuthal angle.] A photon that passes through the center of the aperture projects onto the imaging plane at

$$(x_p, y_p, z_p) = (-b\cot\theta\cos\phi, -b\cot\theta\sin\phi, -b).$$

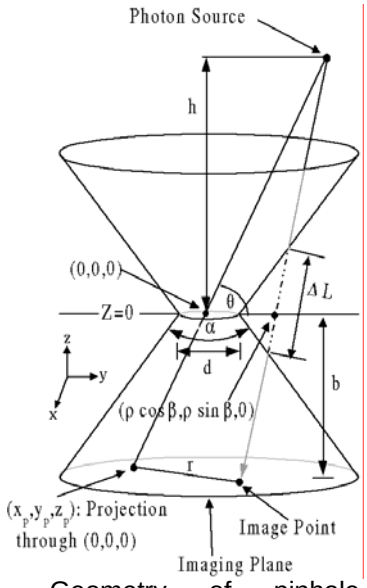

Figure D1. Geometry of pinhole-collimator imaging. The collimator has diameter d and opening angle α. A photon source at angle θ and a distance h above the aperture projects onto the imaging plane at (x_p, y_p, z_p), the center of the point response function (PRF). A photon passing a distance ΔL through attenuating material impinges on the imaging plane a distance r from the center of the PRF. The polar coordinates of the intersection point of this photon with the $z=0$ plane are (ρ,β).

If the photon does not pass through the center of the aperture, it projects onto the imaging plane a distance r from (x_p, y_p, z_p). The photon's path length through attenuating material is ΔL.

$$\Delta L = \frac{\left[\csc^2\theta - \frac{2r}{h+b}\cot\theta\cos(\beta-\phi) + \frac{r^2}{(h+b)^2}\right]^{\frac{1}{2}}}{\tan^2\frac{\alpha}{2} - \cot^2\theta + \frac{2r}{h+b}\cot\theta\cos(\beta-\phi) - \frac{r^2}{(h+b)^2}} \times$$

$$\left\{ -d\tan\frac{\alpha}{2} + \left(\begin{array}{l} \frac{r^2h^2}{(h+b)^2}\left[\tan^2\frac{\alpha}{2} - \cot^2\theta\sin^2(\beta-\phi)\right] + \frac{d^2}{4}\left[\cot^2\theta - \frac{2r}{h+b}\cot\theta\cos(\beta-\phi) + \frac{r^2}{(h+b)^2}\right] \\ -\frac{drh}{h+b}\tan\frac{\alpha}{2}\left[\cot\theta\cos(\beta-\phi) - \frac{r}{h+b}\right] \end{array} \right)^{\frac{1}{2}} \right.$$

$$\left. + \left(\begin{array}{l} \frac{r^2h^2}{(h+b)^2}\left[\tan^2\frac{\alpha}{2} - \cot^2\theta\sin^2(\beta-\phi)\right] + \frac{d^2}{4}\left[\cot^2\theta - \frac{2r}{h+b}\cot\theta\cos(\beta-\phi) + \frac{r^2}{(h+b)^2}\right] + \\ \frac{drh}{h+b}\tan\frac{\alpha}{2}\left[\cot\theta\cos(\beta-\phi) - \frac{r}{h+b}\right] \end{array} \right)^{\frac{1}{2}} \right\} \quad \text{(D.1)}$$

The Point Response Function (PRF) has two components: photons passing through the aperture and photons passing through attenuating material. The PRF is

$$PRF = \begin{cases} \dfrac{\sin^3\theta}{4\pi\left(h+b\right)^2}, \; r \le \dfrac{d(h+b)}{2h} \\ \dfrac{\sin^3\theta}{4\pi\left(h+b\right)^2} e^{-\mu\Delta L}, \; r > \dfrac{d(h+b)}{2h} \end{cases} \tag{D.2}$$

In *[5]*, we also derived analytic expressions for the root-mean-square (RMS) of the PRF. These were compared to results obtained by numerical integrations (see Figure 5 in *[5]*); the theoretical results agreed well with the results obtained by numerical integrations.

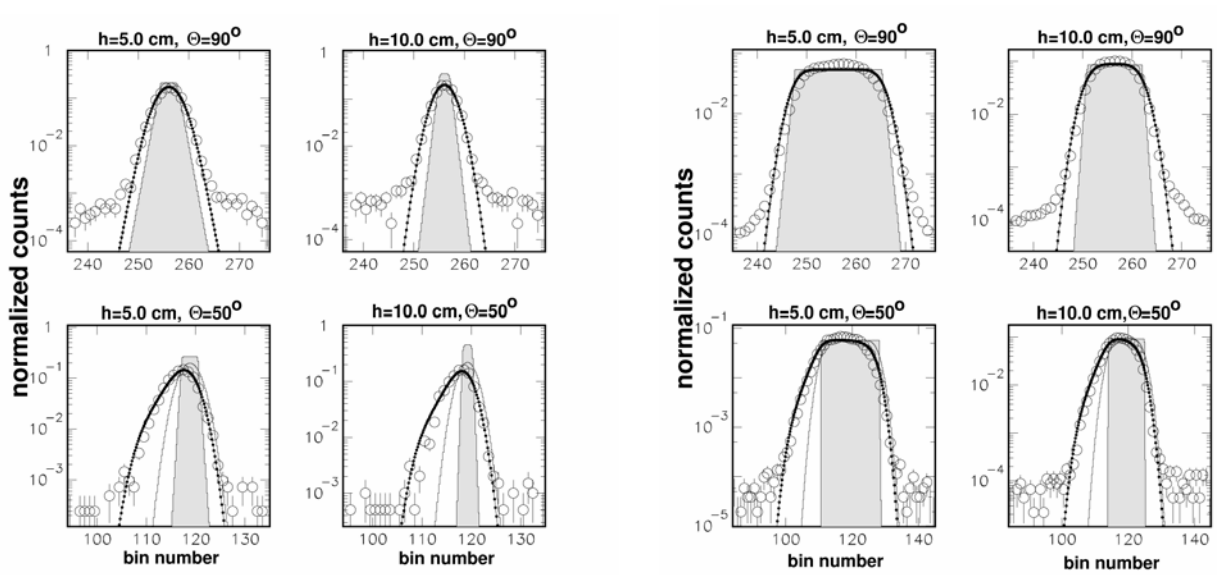

Figure D2. Normalized longitudinal profiles for a Tc-99m source with a 0.77~mm dia. (left) and 4.00mm dia. (right) tungsten aperture. Experimental data (open circles) are shown with the theoretical PRF (shaded histogram). The theoretical curve is then convolved with Gaussian detector resolution of 1.5mm RMS (solid line) and convolved with exponential obliquity and Gaussian detector resolution (small black circles). The heights above the aperture plane are 5.0cm (left) and 10.0cm (right). The acquisition angles are $\theta = 90^o$ (top) and $\theta = 50^o$ (bottom).

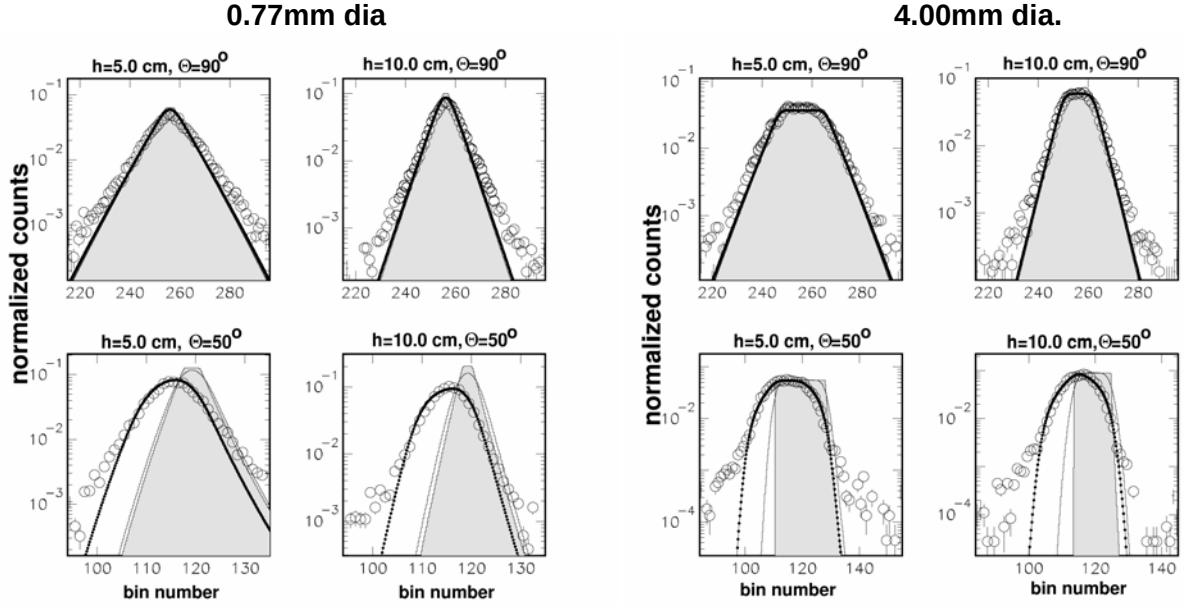

Figure D3. Normalized longitudinal profiles for an I-131 source with a 0.77mm dia. (left) and a 4.00mm-dia. (right) tungsten aperture. The layout is described in Figure D2.

Experimental data have been acquired to test the above theoretical predictions for the pinhole PRF. Two different isotopes (Tc-99m and I-131), two different pinhole aperture diameters (0.77mm and 4.00mm), two different heights (5.0cm and 10.0cm), and two different angles (50^o and 90^o) were used in the test. The results are shown in Figures D2 and D3. The data match the theory well when the theoretical prediction is convolved with both Gaussian detector resolution and with exponential depth-of-interaction (parallax). When an oblique photon is detected, its expected measurement position depends on how much of the crystal the photon penetrates before being captured; this is an exponential process.

Table I in *[5]* compares RMS values obtained from experimental data with the predictions from the analytic equation; their agreement is very good.

E. COMPLETE SAMPLING: THEORETICAL AND COMPUTATIONAL DEVELOPMENTS

During this project period, we have investigated the complete-sampling conditions for orbits of pinhole collimators *[4, 10]*. We have made progress in both complete-sampling theory and also in computational methods.

Tuy *[11]* and others *[12, 13]* have derived a sufficiency condition for complete sampling using a cone-beam geometry. Tuy originally stated his condition as "if on every plane that intersects the object there exists at least one cone-beam source (focal) point, then one can reconstruct the object" *[11]*. Orlov has derived a condition for parallel-beam collimation, stating his condition as the curve of vantage angles on a unit sphere of directions must "have points in common with any arc of a great circle *[14]*." We have found a geometric relationship between these two conditions that is valid even when the focal length of the cone-beam collimator is finite. In the limit of infinite focal length, cone-beam collimation approaches parallel-beam collimation. We have re-written the Tuy condition using the language of Orlov: "For all voxels in the completely sampled volume, the set of vantage angles on a unit sphere of directions, from each voxel to each point on the curve of focal points, must "have points in common with any arc of a great circle *[14]*."

We have used the re-written condition to develop a numerical algorithm for evaluating the largest completely sampled region (LCSR) for a given orbit. The algorithm uses a digital representation of the vantage angles to determine if a voxel meets the re-written condition. The set of untruncated voxels that meet the re-written condition forms the largest completely sampled volume.

E.1. Examples

The program has been tested using parallel-beam collimators, slant-hole collimators, cone beam, and pinhole collimators. Examples of completely sampled volumes are described below.

E.1.1. Parallel-Beam Collimators with Circular Orbits

Parallel-beam collimators with untilted circular 360^o orbits have been evaluated on a 64^3 grid of 0.712-cm-wide voxels and produce cylindrical LCSRs, as expected. A transaxial slice of an LCSR is shown in Figure E1(a). For this LCSR, the gamma camera dimensions were 45.6cm transaxially and 22.8cm axially; the radius of rotation was 30.0cm.

The LCSR of a parallel-beam collimator following a 360^o circular orbit depends only on the detector dimensions and not the orbit dimensions. That volume is cylindrical with magnitude $\pi w^2 d/4$, where w is the transaxial width of the detector and d is the axial depth of the detector. The LCSR volume predicted by the formula is $37{,}157\text{cm}^3$. The volume determined by the program was $38{,}670\text{cm}^3$, which is larger than expected by 4%, presumably because of binning effects.

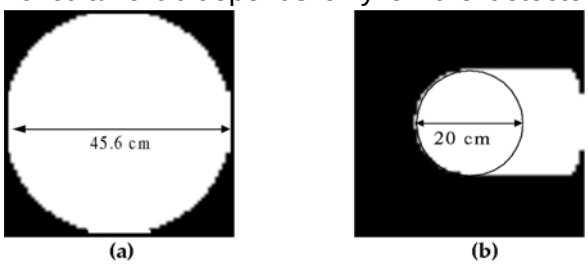

Figure E1. (a)Transaxial slice of the LCSR for parallel-beam collimator with a 360^o circular orbit. The volume is cylindrical with a diameter of 45.6cm. (b)Transaxial slice of the LCSR for parallel-beam collimator with a 180^o circular orbit.

Figure E1(b) shows the LCSR for a semicircular (180^o) orbit of a parallel-beam collimator. It is asymmetric. Halfway through the 180^o orbit, the camera has a view to the right. The ROR was 10.0cm. The calculated volume was $14{,}761\text{cm}^3$. The expected volume was

$$\frac{w^2}{4}\sin^{-1}\frac{20}{w}+\frac{20}{4}\sqrt{w^2-20^2}+\frac{20^2}{8}\pi=13{,}634\text{ cm}. \qquad \text{(E.1)}$$

Figure E2. LCSR for helical plus half-circle pinhole-collimator orbit. Transaxial (a) and sagittal (b) slices through the LCSR are shown. The volume is nearly cylindrical, except for defects at the ends (b, bottom), where the valid volume depends on the initial angle of acquisition, and except for binning effects. The axial translation of the orbit is 1.28~cm, which corresponds to two bins. The volume is three bins wide axially due to edge effects and centering.

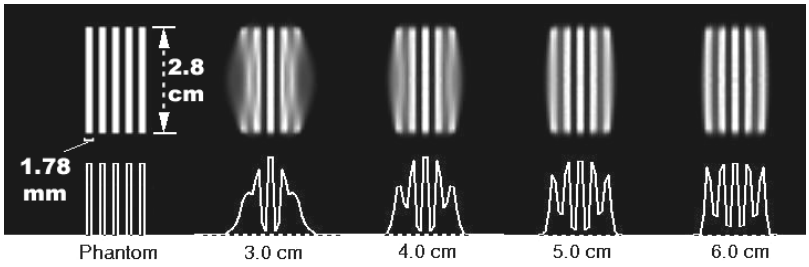

Figure E3: Comparison of simulated circular orbits with different RORs. On the far left, the central coronal slice of the digital phantom (top) and its profile (bottom) are shown. The phantom has five hot disks separated by four cold disks. The disks are 1.78mm thick. Simulated data were reconstructed for RORs of 3.0, 4.0, 5.0, and 6.0cm, respectively, from left to right. The central coronal slices (top) and their profiles (bottom) are shown.

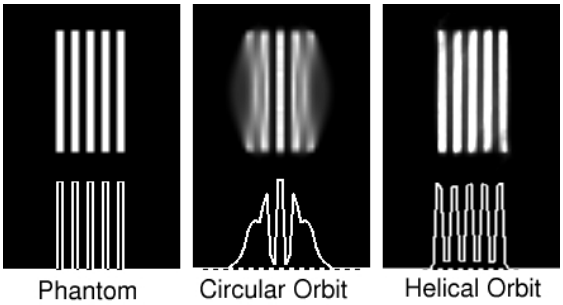

Figure E4. Helical-orbit simulation. The central coronal slice of reconstructions from simulated circular-orbit (middle) and helical-orbit (right) data are shown with their profiles (bottom). The digital phantom used to simulate the projection data is on the left. The ROR was 3.0cm for the two orbits. The helical orbit had an axial travel of 2.0cm, centered on the central slice of the phantom. The bin size is 0.89mm.

E.1.2. Pinhole Collimators

The pinhole collimator has also been tested with a 192-view helical orbit and produces a nearly cylindrical LCSR using a 64^3 grid of 0.712cm-wide voxels (Figure E2). The orbit included a 128-view helical orbit with a 10cm ROR traversing 1.28cm along the axis of rotation followed by a 64-view half-circular orbit at the far end of the helix. The defects in the cylinder are at the ends, as expected, because of the strong dependence on the initial orientation of the camera. The total volume determined by the program was 368cm^3.

E.2. Helical Pinhole Studies

Pinhole collimation has similar complete sampling properties to cone-beam collimation. Complete sampling of an object cannot be obtained from the circular rotation of the aperture about the object. We have investigated helical pinhole SPECT scans as a method of obtaining completely sampled data *[3, 15]*.

We have performed simulations of pinhole acquisition using a disk phantom to study the effect of radius of rotation (ROR) on axial blurring. The simulated disk phantom had a disk diameter of 2.8cm and a disk thickness of 1.78mm. Projection data were simulated and then reconstructed. Figure E3 shows reconstructions of simulated projection data using a circular scan for different values of ROR. The simulation shows that axial blurring is worse for smaller RORs. This is very unfortunate because both sensitivity and resolution are improved at smaller RORs. Helical orbits were evaluated because they offer the potential of a small ROR for high sensitivity and resolution combined with complete sampling. Figure E4 is a comparison of reconstructions from simulated circular-orbit and simulated helical-orbit projection data.

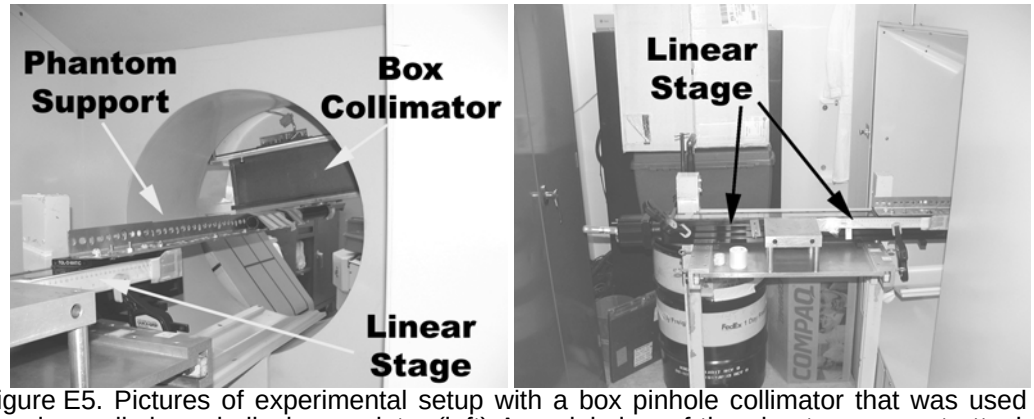

Figure E5. Pictures of experimental setup with a box pinhole collimator that was used to acquire preliminary helical scan data. (left) An axial view of the phantom support attached to the linear stage during a scan is shown on the left. (right) Side view of linear stage.

We obtained experimentally acquired data by using the

existing research scanner, which gives a circular orbit of a pinhole collimator and by using a linear stage to give axial translation of the phantom. A picture of the setup is shown in Figure E5.

The experimental data were reconstructed. The resulting reconstructions are shown in Figure E6. We have estimated our experimental axial resolution to be about 0.9mm by using a least-square comparison with a digital phantom with convolved Gaussian resolution. The Gaussian resolution was varied until the squared difference was minimized.

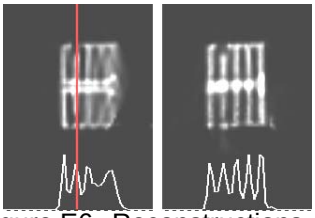

Figure E6. Reconstructions of experimental data. The central coronal slices of reconstructions from experimentally acquired single circular-orbit (left) and helical-orbit (right) projections are shown in the top row. Their corresponding profiles are shown in the bottom row. The red line indicates the plane of the aperture for the circular orbit.

F. PINHOLE CALIBRATION STUDIES

We have begun a study of the effects of mechanical and electronic shifts on reconstruction that suggests that even very small shifts (a fraction of a millimeter) can introduce substantial artifacts in the reconstruction.

F.1. Definition of Mechanical and Electronic Shifts

Figure F1 shows a pinhole collimator, the axis of rotation (AOR), and a point source at (x_0,y_0,z_0). The radius of rotation (ROR) and the focal length (FL) are indicated. The point source projects onto the imaging plane (Y=ROR+FL) at $(x_1,ROR+FL,z_1)$. The mechanical and electronic shifts (defined below) determine the expected projection position of the point source.

F.1.1. Mechanical Shifts

Mechanical shifts are a property of the aperture and determine the position of the center of the aperture relative to the AOR. The central plane is the plane perpendicular to the detector plane that contains the AOR. In a well aligned system, that plane would also contain the center of the aperture. The transaxial mechanical offset (τ_x) is the distance from this plane; τ_x is the dot product of a vector from the central plane to the center of aperture with the unit vector in the *x* direction. The transaxial mechanical shift can be defined because there is a reference point: the AOR.

The axial mechanical shift (τ_z) cannot be well defined for a single pinhole collimator. The reason for this is that the mechanical shift can be absorbed into the electronic shift; the two shifts cannot be separated for a single pinhole collimator. However, when there are multiple cameras each with a pinhole aperture, one can define the axial origin. This can be done, for example, by defining the mechanical shift of the first collimator to be zero. Other collimators will have a relative shift; this allows a decoupling of the axial mechanical and electronic shifts.

F.1.2. Electronic Shifts

Electronic shifts are a property of the detector and determine the readout position of a photon. The electronic shift is the difference between the actual electronic readout of a particular physical position on the detector and the expected readout of that position. If a source is collimated in the central plane and perpendicular to the detector, the expected transverse electronic readout is zero. The actual transverse readout is the transverse electronic shift (ε_x). A shift of zero refers to a well calibrated electronic system. Electronic shifts may be corrected by shifting the projection data; mechanical shifts may not be corrected this way.

The axial electronic shift (ε_z) for a one collimator system is the difference between the actual axial readout position of a line perpendicular to the detector and through the aperture and the expected readout for an aperture centered above the detector. For multiple collimators, it is possible to separate electronic and mechanical shifts.

F.2. Calibration with Radionuclide Point Source

Calibration with a line source has previously been used successfully for fan-beam, cone-beam and pinhole collimation *[16-19]*. We have developed a similar technique to calibrate either a single or multiple pinhole collimators by rotating the collimator around a point source. We have determined the expected position of the projection data as a function of gantry angle, source position, and both the mechanical and electronic shift. We then calculate the centroid of the experimental calibration scan as a function of gantry

angle and then fit the centroids to determine the position of the source and the mechanical and electronic shifts.

Figure F1 shows that the position of the source is (x_0,y_0,z_0). The position of the aperture is (τ_x, ROR, τ_z). When the gantry rotates from its original position by an angle ϕ, the point source is at $(x_0\cos\phi + y_0\sin\phi, y_0\cos\phi - x_0\sin\phi, z_0)$ relative to the detector; this is equivalent to the object rotating by $-\phi$ for a stationary detector. The detected centroid is located at $(x_1,ROR+FL,z_1)$. The vector from the source to the aperture is

$$\overrightarrow{\Delta_1} = (\tau_x - x_0\cos\phi - y_0\sin\phi, ROR + x_0\sin\phi - y_0\cos\phi, \tau_z - z_0)$$

. A second vector $\overrightarrow{\Delta_2}$ is the displacement from the physical aperture to the detector plane. The two vectors are related by the following equation: $\overrightarrow{\Delta_2} = k\overrightarrow{\Delta_1}$, where $k = FL/(ROR + x_o\sin\phi - y_o\cos\phi)$. This value of k is the ratio of the y distance from the aperture to the detector plane and the distance from the point source to the aperture. The expected intersection of the photon with the detector plane is then

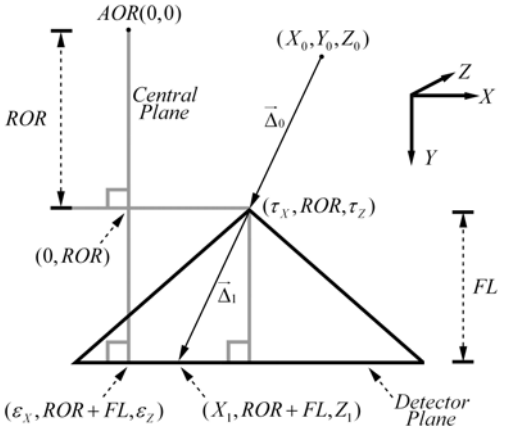

Figure F1: Schematic representation of mechanical and electronic shifts. The mechanical and electronic shifts are defined with respect to the axis of rotation (AOR). The figure shows a transverse view. A point source at *(X_0, Y_0, Z_0)* and its projection are also shown. The mechanical shift is exaggerated for clarity.

$$\left(\tau_x + \frac{FL(\tau_x - x_0\cos\phi - y_0\sin\varphi)}{ROR + x_0\sin\phi - y_0\cos\varphi}, ROR + FL, \tau_z + \frac{FL(\tau_z - z_0)}{ROR + x_0\sin\phi - y_0\cos\varphi}\right). \quad \text{(F.1)}$$

When electronic shifts $(\varepsilon_x, \varepsilon_z)$ are taken into account, the expected readout position is

$$\left(\tau_x + \varepsilon_x + \frac{FL(\tau_x - x_0\cos\phi - y_0\sin\varphi)}{ROR + x_0\sin\phi - y_0\cos\varphi}, ROR + FL, \tau_z + \varepsilon_z + \frac{FL(\tau_z - z_0)}{ROR + x_0\sin\phi - y_0\cos\varphi}\right). \quad \text{(F.2)}$$

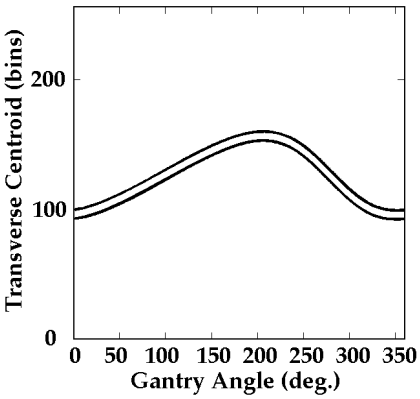

Figure F2: Experimental transverse projection data (open black circles) and fit of eqn. (F.1) to data (white line). The centroid of each projection view was used in the fit and shown in the plot. Since there are many circles, the data points appear as a solid black band.

One should note that the z term does not allow separation of τ_z and z_0; hence, it is not possible to separate the axial mechanical and electronic shifts. For example, by increasing τ_z and z_0 by the same amount ε_z is decreased, the expected z position remains unchanged. For one collimator, τ_z may be set to zero (the axial origin then coincides with the aperture); then both the electronic shift and the z position of the source can be determined. For multiple pinhole collimators (each with one aperture), setting the first axial mechanical shift to zero allows the determination of τ_z for the other collimators; all the electronic shifts can thus be determined.

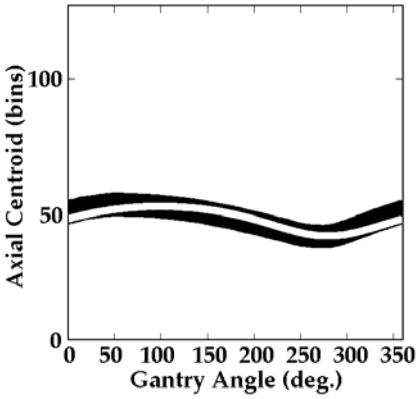

Figure F3: Experimental axial projection data (open black circles) and fit of eqn. (F.1) to data (white line). The centroid of each projection view was used in the fit and shown in the plot. Since there are many data points, the circles appear as a solid black band.

F.3. Experimental Results

We have acquired experimental calibration data. We fitted the centroids simultaneously to the expected x and z components of Equation (F.2). The variables x_0, y_0, z_0, τ_x, ε_x, and ε_z were determined using a maximum likelihood fit. The data and the fit are shown in Figures F2 and F3. The data show good

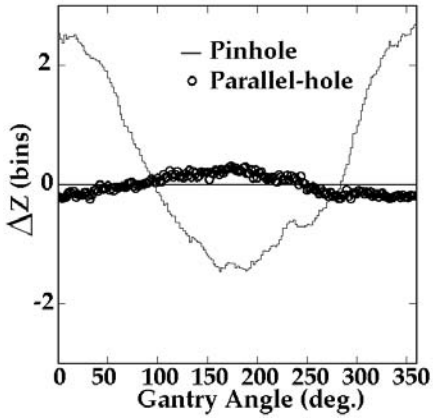

Figure F4: Difference between experimental slice (z) and expected slice (z) from fit. Pinhole data (solid line) and parallel-data (open black circles) are shown. The difference in direction and difference in magnitude (pinhole approximately 5x parallel-hole) suggests a mechanical tilt of the heads as a function of gantry angle.

agreement with expectation. The difference between the z data and the fit is shown in Figure F4. The difference has an approximately sinusoidal nature; it is angular-dependent. *("angular dependent" will refer to quantities that are not constant with respect to change in the gantry angle)*. For comparison, the z centroid data of a parallel-hole collimator are also shown in Figure F4. The sinusoidal nature is still present, except that the curve is inverted and the relative magnitude is approximately ROR/FL; this suggests there is a mechanical tilt in the new scanner. We attempted to measure the tilt of the collimator using a hand-held digital level with 0.1^o precision, but we were not able to measure a tilt. However, if the oscillation is due to a mechanical tilt of the collimator, a shift of about 0.1^o is sufficient to introduce a 2.5mm shift. In addition, we measured the tilt with respect to gravity. We will need to locate the AOR with a laser to determine if it is perpendicular to gravity. It is possible in our case that the AOR is slightly tilted (about 0.1^o) with respect to gravity, and that the tilt of the collimator at its highest and lowest points compensates to give an approximately level collimator, to the precision of the level. It is likely that all scanners have tilts; the magnitude will vary substantially. The amplitude of the projection is about 1.5 bins (about 2.5mm) for the pinhole collimator. This type of problem can substantially degrade resolution. It is exactly the type of problem that this DOE grant attempts to solve by introducing angular-dependent calibration corrections.

F.4. Reconstruction of Cold-Rod Phantom with Calibration Information

Experimental data were acquired using a micro cold-rod phantom. Calibration information was obtained by performing a 360^o scan of a point source and fitting the projection centroid. By fitting to Equation (F.2), the transverse mechanical shift was estimated to be -0.61mm. We found that the electronic shift was 0.04mm, which was within one standard deviation of zero. Holding the electronic shift constant at 0.04mm, we performed three reconstructions, as seen in Figure F5. The left image used the estimated mechanical shift in the reconstruction. The center image used no compensation. The right image used 0.61mm (instead of -0.61mm).

The reconstruction program we used was the same one used to estimate resolution degradation; it models spatially varying sensitivity and constant detector resolution (4.5mm full width at half maximum (FWHM)). This relatively large value was used as an attempt to compensate for aperture size and penetration, which are not otherwise modeled by this reconstruction program. The program does not model spatially varying resolution, as our more sophisticated reconstruction program does. Unfortunately, that program does not yet have compensations for mechanical and electronic shifts. In addition, the program used for these reconstructions reconstructed only the central axial slice; it was a 2D reconstruction.

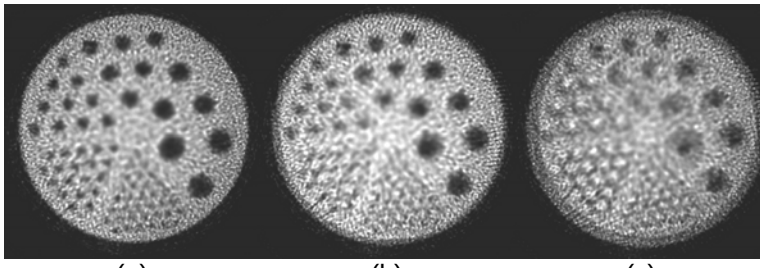

(a) (b) (c)

Figure F5: Experimental reconstructions of micro cold-rod phantom using a simplified iterative reconstruction. A transaxial slice is shown for mechanical shift correction in the correct direction (a), no correction (b), and the wrong direction (c). Rod diameters are about 1.0, 1.6, 2.4, 3.2, 4.0, and 4.8mm.

Despite the drastic simplifications in the reconstruction program, there is a remarkable difference in image quality between the three images. For (a), the 1.6mm rods are clearly visible and the 1.0mm rods are also visible. For (b), the 2.4mm rods are visible. Artifacts obscure the 1.6mm rod. For (c), there are hints of the 3.2mm rods, which should appear as solid black circles. There are severe artifacts in this reconstruction; some rods erroneously appear as hot rods. This dramatic difference is due to an uncompensated mechanical shift of just 0.61mm.

F.5. Effect of Mechanical and Electronic Shifts on Reconstruction Resolution

A digital hot-rod phantom was used to generate simulated projection data of a pinhole collimator following a circular orbit (ROR=5.0cm; FL=15.0cm). The simulation allowed for the introduction of both mechanical and electronic shifts in the projection data. The simulation did not model spatially varying resolution or aperture penetration, but it did model detector resolution (Gaussian, 1.0mm FWHM). The projections were reconstructed using MLEM without accounting for mechanical or electronic shifts; this typically introduced artifacts into the reconstruction as seen in Figure F6. For small shifts, the resolution degradation can be estimated by determining the least squared difference between the reconstruction and the phantom after it is convolved with Gaussian resolution. Figures F7 and F8 show the resolution degradation for mechanical and electronic shifts, respectively. The resolution has been deconvolved with the zero-shift resolution (0.088mm) so that the degradation at zero shift is zero. The resolution values shown are the FWHM values for Gaussian resolution.

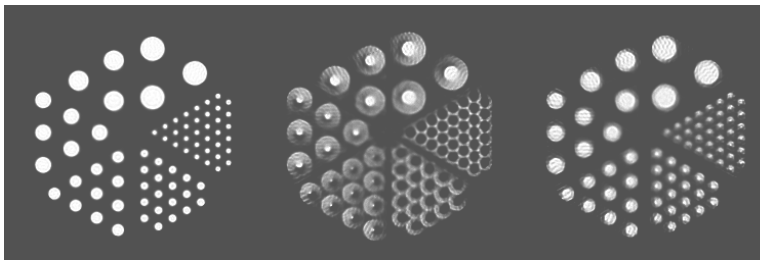

(a) (b) (c)

Figure F6: Comparison of reconstruction from simulated hot-rod projections with no shift (a), 1.0mm mechanical shift (b), and 1.0mm electronic shift (c). Pixel size was 200 microns. 250 iterations of MLEM were used.

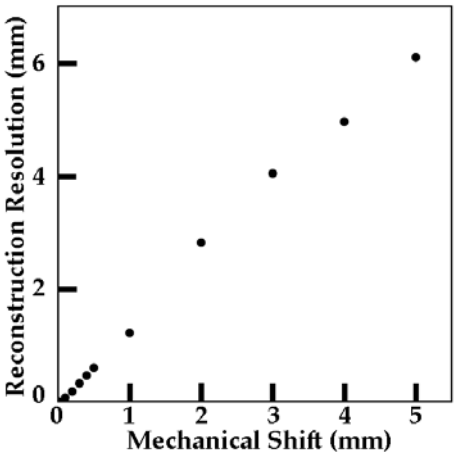

Figure F7: Resolution degradation (FWHM) versus mechanical shift for a cold-rod phantom.

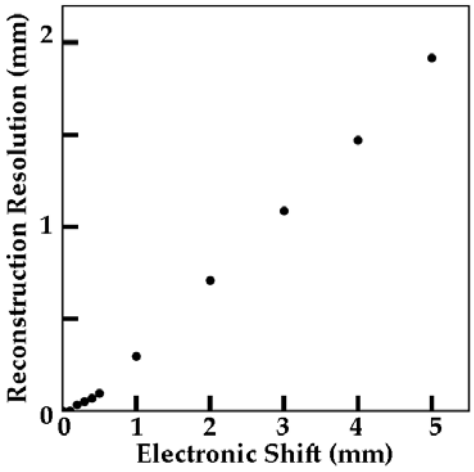

Figure F8: Resolution degradation (FWHM) versus electronic shifts for cold-rod phantom.

G. LITERATURE CITED

[1] Metzler SD, Bowsher JE, Smith MF, Jaszczak RJ. Analytic determination of pinhole collimator sensitivity with penetration. *IEEE Transactions on Medical Imaging* 2001; 20:730-741.
[2] Pieper BC, Metzler SD, Bowsher JE, Jaszczak RJ. Single and double knife-edge pinhole collimators for SPECT imaging of small volumes. *Journal of Nuclear Medicine* 2002; 43:223P-224P.
[3] Metzler S, Pieper B, Greer K, Jaszczak R. Improving pinhole SPECT sampling through spiral orbits. *Journal of Nuclear Medicine* 2002; 43:10P.
[4] Metzler S, Bowsher J, Pieper B, Greer K, Jaszczak R. Improving pinhole SPECT reconstruction through modeling. *Journal of Nuclear Medicine* 2002; 43:105P.
[5] Metzler SD, Bowsher JE, Greer KL, Jaszczak RJ. Analytic determination of the pinhole collimator's point-spread function and RMS resolution with penetration. *IEEE Transactions on Medical Imaging* 2002; 21:878-87.
[6] Metzler SD, Bowsher JE, Greer KL, Jaszczak RJ. *Analytic determination of the pinhole collimator's point-spread function and RMS resolution with penetration*. in *2001 IEEE Nuclear Science Symposium*. 2002. San Diego, CA:
[7] Smith MF, Jaszczak RJ. A rotating parallel hole collimator for high resolution imaging of medium energy radionuclides. *IEEE Transactions on Nuclear Science* 1998; 45:2102-2112.
[8] Gonzalez Trotter D, Bowsher J, Jaszczak R. Absolute quantitation of a spherical I-131 activity distributions using a high-resolution rotating collimator: A phantom study. *IEEE Transactions on Nuclear Science* 2001; 48:65-73.
[9] Gonzalez Trotter DE, Jaszczak RJ, Bowsher JE, Akabani G, Greer KL. High-resolution absolute SPECT quantitation for I-131 distributions used in the treatment of lymphoma: A phantom study. *IEEE Transactions on Nuclear Science* 2001; 48:707-714.
[10] Metzler SD, Bowsher JE, Jaszczak RJ. *Geometrical similarities of the Orlov and Tuy sampling criteria and a numerical algorithm for assessing sampling completeness*. in *2002 IEEE Nuclear Science Symposium*. 2002. Norfolk, VA:
[11] Tuy HK. An inversion formula for cone-beam reconstruction. *SIAM Journal on Applied Mathematics* 1983; 43:546-552.
[12] Kirillov AA. On a problem of I.M. Gel'fand. *Sov. Math. Dokl. (English Translation)* 1961; 2:268-269.
[13] Smith BD. Image reconstruction from cone beam projections: Necessary and sufficient conditions and reconstruction methods. *IEEE Transactions on Medical Imaging* 1985; MI-4:14-25.
[14] Orlov S. Theory of three dimensional reconstruction. *Kristallografiya* 1975; 20:511-515.
[15] Metzler SD, Greer KL, Jaszczak RJ. Helical pinhole SPECT for small-animal imaging: A method for addressing sampling completeness. *IEEE Transactions on Nuclear Science* 2003; 50:1575-1583.
[16] Li J, Jaszczak RJ, Coleman RE. Maximum likelihood reconstruction for pinhole SPECT with a displaced center of rotation. *IEEE Transactions in Medical Imaging* 1995; 14:407-409.
[17] Li J, Jaszczak RJ, Coleman RE. *Maximum likelihood reconstruction for converging beam SPECT with a displaced center-of-rotation*. in *IEEE Nuclear Science Symposium and Medical Imaging Conference*. 1993. San Francisco, CA: IEEE.
[18] Li J, Jaszczak RJ, Greer KL, Coleman RE. A filtered backprojection algorithm for pinhole SPECT with a displaced centre of rotation. *Physics in Medicine & Biology* 1994; 39:165-176.
[19] Gullberg GT, Crawford CR, Tsui BMW. Reconstruction algorithm for fan beam with a displaced center-of-motion. *IEEE Transactions on Medical Imaging* 1986; 5:23-29.